

Hydrophilic Microporous Membranes for Selective Ion Separation and Flow-Battery Energy Storage

Rui Tan^{1,9}, Anqi Wang^{1,9}, Richard Malpass-Evans², Evan Wenbo Zhao³, Tao Liu^{3,8}, Chunchun Ye², Xiaoqun Zhou¹, Barbara Primera Darwich¹, Zhiyu Fan¹, Lukas Turcani⁴, Edward Jackson⁴, Linjiang Chen⁵, Samantha Y. Chong⁵, Tao Li⁶, Kim E. Jelfs⁴, Andrew I. Cooper⁵, Nigel P. Brandon⁷, Clare P. Grey³, Neil B. McKeown^{2*}, Qilei Song^{1*}

¹Barrer Centre, Department of Chemical Engineering, Imperial College London, London SW7 2AZ, UK.

²EaStChem School of Chemistry, University of Edinburgh, Edinburgh, EH9 3FJ, UK.

³Department of Chemistry, University of Cambridge, Cambridge CB2 1EW, UK.

⁴Department of Chemistry, Imperial College London, London SW7 2AZ, UK.

⁵Department of Chemistry/ Materials Innovation Factory, Leverhulme Research Centre for Functional Materials Design, University of Liverpool, Liverpool L7 3NY, UK.

⁶Department of Chemistry and Biochemistry, Northern Illinois University, DeKalb, IL, USA & X-ray Science Division, JCESR, Argonne National Laboratory, Lemont, IL60439, USA.

⁷Department of Earth Science and Engineering, Imperial College London, London SW7 2AZ, UK.

⁸Present address: Shanghai Key Laboratory of Chemical Assessment and Sustainability, Department of Chemistry, Tongji University, Shanghai 200092, P. R. China.

⁹These authors contributed equally.

Email: Neil.McKeown@ed.ac.uk, q.song@imperial.ac.uk

Abstract

Membranes with fast and selective ion transport are widely used for water purification and devices for energy conversion and storage including fuel cells, redox flow batteries, and electrochemical reactors. However, it remains challenging to design cost-effective, easily processed ion-conductive membranes with well-defined pore architectures. Here, we report a new approach to designing membranes with narrow molecular-sized channels and hydrophilic functionality that enable fast transport of salt ions and high size-exclusion selectivity towards small organic molecules. These membranes, based on polymers of intrinsic microporosity (PIMs) containing Tröger's base or amidoxime groups, demonstrate that exquisite control over subnanometer pore structure, the introduction of hydrophilic functional groups, and thickness control all play important roles in achieving fast ion transport combined with high molecular selectivity. These membranes enable aqueous organic flow batteries with high energy efficiency and high capacity retention, suggesting their utility for a variety of energy-related devices and water purification processes.

In addition to conventional membrane separation processes^{1,2}, there is a rapidly growing demand for ion-transport membranes in applications related to energy¹⁻³. With greater reliance on renewable but intermittent energy sources such as solar and wind power, energy conversion and storage technologies are required to integrate low-carbon energy into the power grid. These include electrochemical water splitting and electrolysis for H₂ production⁴, proton-exchange membrane (PEMs) and alkaline fuel cells for energy conversion⁵, electrochemical reduction of CO₂ and N₂ to fuel and chemicals⁶, and scalable redox flow batteries (RFBs)^{3,7}. In all of these established and emerging electrochemical processes, ion-selective membranes transport ions whilst isolating the electrochemical reactions in separate cells. In the new generation of RFBs⁸⁻¹⁴, low-cost and high-performance membranes need to have precise selectivity between ions and organic redox-active molecules¹⁵⁻¹⁸.

Whilst various new electrochemical processes have been developed, the use of expensive commercial ion-exchange membranes, such as the poly(perfluorosulfonic acid) (PFSA)-based Nafion (~\$500 per m²),

dominate, despite suffering from poor selectivity due to swelling in water. Intensive research efforts have developed low-cost hydrocarbon-based polymer electrolyte membranes^{5, 19,20,21}, for example, polyaromatic ionomers with pendant ionic functional groups demonstrate promising performance in vanadium flow batteries^{22, 23} and fuel cells²⁴⁻²⁶. Ion transport within these polymers depends on the formation of nanoscale interconnected water channels via microphase separation of the hydrophobic backbone and hydrophilic side chains,²⁹ which is a complex process that is difficult to control on a molecular level. Hence, the key scientific challenge for obtaining highly-selective ion-transport membranes is the design of processable materials that achieve precise control over pore architecture, pore size distribution, and ionic conductive functionality^{2, 27-35}.

Here, we demonstrate a new approach for the design of ion-selective membranes based on hydrophilic polymers of intrinsic microporosity (PIMs)³⁶⁻³⁸ that enable fast ion transport and high molecular selectivity (Fig. 1a). Our innovative strategy combines: (i) the use of PIMs to provide rigid and contorted polymer chains that pack inefficiently so as to generate microporosity with narrow pore size distribution; (ii) the incorporation of hydrophilic functional groups (including ionizable groups) that generate interconnected water channels for ion-conductivity; and (iii) solution processing to give thin films with submicron thickness that further reduces ion transport resistance and membrane production costs. We demonstrate the selective ion separation of these microporous membranes and their application within efficient and stable aqueous organic redox flow batteries.

Synthesis and characterization of hydrophilic microporous membranes

Figure 1b shows the conceptual diagram of the interconnected hydrophilic ionic channels in the microporous membranes fabricated from a hydrophilic PIM polymer (Fig. 1c). To realise our design strategy, we developed two types of hydrophilic PIMs firstly, PIMs derived from Tröger's base (TB-PIMs) and, secondly, dibenzodioxin-based PIMs with hydrophilic and ionizable amidoxime groups (AO-PIMs) (Fig. 1d). Details of PIM synthesis (Fig. S1) and spectroscopic characterisation (Fig. S2-S3) are provided in the Methods Section and the Supplementary Information. The three TB-containing polymers selected for investigation were based on ethanoanthracene (*i.e.*, PIM-EA-TB), benzo-methanoanthracene (*i.e.*, PIM-BzMA-TB) and dimethylbiphenyl (*i.e.*, DMBP-TB), which provide a range of microporosity (Fig. 2a), as measured by gas adsorption, with apparent BET surface areas of 977, 808 and 325 m² g⁻¹, respectively. A

simulation of the pore structure provided by the inefficient packing of polymer chains is shown in Fig. 1c for PIM-EA-TB. In addition, amidoxime-modified PIMs were prepared using a controlled reaction of the nitrile groups in PIM-1 with hydroxylamine³⁹, to give 32, 56, 63, 83 and 100% conversions and PIM-SBF^{40, 41} with 100% conversion. N₂ gas adsorption isotherms (Fig. 2d) show that the AO modification leads to a drop of BET surface area from 778 m² g⁻¹ (PIM-1) to 567 m² g⁻¹ (AO-PIM-1), likely due to hydrogen bonding interactions⁴² that leads to tighter chain packing and the creation of more ultramicropores (i.e. of diameter <7 Å), whilst retaining overall high micropore volume (0.194 cm³ g⁻¹). Pore size distributions derived from CO₂ adsorption isotherms confirm that the pores in PIM-EA-TB and AO-PIM-1 are predominately sub-nanometre in diameter (Extended Data Fig. 1). Atomistic molecular dynamics (MD) simulations suggest a narrow pore size distribution in the range of 2-8 Å (Fig. 1e, Extended Data Fig. 2).

Thick self-supported PIM membranes were fabricated by solution-casting (Fig. 1f, Extended Data Fig. 3) and thin film composite membranes of PIM-EA-TB, PIM-BzMA-TB and DMBP-TB (~350 nm) were also prepared by spin-coating or blade-coating a dilute polymer solution onto a low-cost porous membrane support (Fig. 1g). The membranes were characterised using gas permeation (Table S1) and scanning electron microscopy (SEM), which confirms the defect-free cross-section of both thick films (Fig. 1f, Fig. S4-5) and thin film composite membranes (Fig. 1h, Fig. S6). The long-term chemical stability of PIM polymers towards strong alkaline solutions was confirmed by Fourier Transform-Infrared (FTIR) spectroscopy and gel permeation chromatography (GPC), which showed that the molecular weight distribution remained unchanged; the maintenance of microporosity was also confirmed by N₂ adsorption (Extended Data Fig. 4). Cyclic voltammetry (CV) indicated good electrochemical stability (Fig. S7). Thermogravimetric analysis (TGA) verified the good thermal stability with no obvious weight loss up to 150 °C (Fig. S8). The mechanical properties of the polymer membranes were measured by nanoindentation using atomic force microscopy (AFM) and tensile tests (Fig. S9-10). The Young's modulus and ultimate tensile strength (Table S2) of PIM-EA-TB and AO-PIM-1 films are as high as 2.0 GPa and 40 MPa, respectively, both higher than those of Nafion membranes (0.3 GPa and 25 MPa). These results suggest that PIM membranes possess high chemical stability, electrochemical stability, thermal stability and mechanical strength.

Water uptake and ionic conductivity

To demonstrate the effect of porosity on water sorption and transport,^{5, 15, 19, 43, 44} we analysed a range of hydrophilic TB-PIMs with different microporosity using dynamic vapour sorption (DVS). For PIM-EA-TB, the combination of high porosity and hydrophilicity of the amine groups within the TB unit enables the polymer to adsorb up to 41.3 wt.% water vapor at 298 K and 30.0 mbar (Fig. 2b, Fig. S11), in contrast, the less porous DMBP-TB adsorbs only 11.3 wt%. Hydrophilicity also promotes the formation of water channels as demonstrated by a comparison of the microporous, hydrophobic PIM-1 with its hydrophilic derivative AO-PIM-1. Despite its high surface area of 778 m² g⁻¹ and micropore volume of 0.251 cm³ g⁻¹, PIM-1 adsorbs only 5.7 wt% of water vapour (Table. S3), whereas the uptake of water vapour in AO-PIM-1 increases linearly from 5.7 to 29.0 wt% on increasing the AO content from 0 to 100 %, (Fig. S11). AO-PIM-SBF with higher porosity (Fig. 2d) adsorbed water vapor up to 34.0 wt.% (Fig. S11). Bulk water uptake was also measured and showed a similar trend (Fig. 2e). Kinetic analyses suggest that water adsorption of PIM membranes follows the clustering mechanism⁴⁴ (Fig. S12). The microstructural changes of PIM membranes on hydration were investigated by wide-angle and small-angle X-ray scattering (Fig. S13-14), which suggest the presence of a continuous network of ultra-micropores in both dry and hydrated states.

Ionic conductivity of thick (50-80 μm) membranes of the three TB-PIM polymers was measured using electrochemical impedance spectroscopy (EIS) over a temperature range of 30-80°C (Fig. 2c and Fig. S15-16). At 30°C, PIM-EA-TB demonstrates an ionic conductivity of 4.4×10^{-4} S cm⁻¹ in 1 M NaOH solution and a comparable value of 2.9×10^{-4} S cm⁻¹ in 1 M NaCl solution. In contrast, lower conductivities in NaOH solution were obtained for PIM-BzMA-TB (4.1×10^{-5} S cm⁻¹) and less porous DMBP-TB (3.1×10^{-6} S cm⁻¹). The Arrhenius-type temperature dependence of ion-conductivity suggests it is controlled by thermally-activated confined water dynamics in the microporous and hydrophilic polymer. Although these intrinsic ionic conductivities are low relative to those of the benchmark ion-exchange membranes such as Nafion, the thin film composite membrane of PIM-EA-TB (300-400 nm) demonstrates a resistance of only $1.2 \Omega \text{ cm}^2$ in 1 M NaOH solution at 25°C. EIS demonstrated that the fully converted 50-μm-thick AO-PIM-1 membranes achieve superior ionic conductivity (4.8×10^{-3} S cm⁻¹). The more porous AO-PIM-SBF with a BET surface area of 618 cm² g⁻¹ achieves even higher ionic conductivity of 8.9×10^{-3} S cm⁻¹ in 1 M NaOH solution at 30°C and 2.1×10^{-2} S cm⁻¹ at 80°C, which are comparable or superior to those of Nafion 212

($1.1 \times 10^{-2} \text{ S cm}^{-1}$ at 30°C and $1.7 \times 10^{-2} \text{ S cm}^{-1}$ at 80°C) (Fig. 2f, S17, Extended Data Fig. 5a, Table S4).

The high ionic conductivity of AO-PIMs in alkaline electrolytes can be ascribed to the introduction of negative charges due to the deprotonation of the amidoxime group ($pK_a \sim 13.2$) at high pH^{45} , which facilitates the transport of positively charged cations (Extended Data Fig. 5, and Supplementary Information Section 3.1.1.). The incorporation of Na^+ in AO-PIM-1 after NaOH treatment was confirmed by XPS spectra whereas NaCl treated AO-PIM-1 and NaOH treated PIM-EA-TB showed no evidence of Na^+ uptake (Fig. S18). The high ionic conductivity in AO-PIMs suggests that the local mobility of water and ions in the micropores and channels is a collective property resulting from the combination of high micropore volume, a large amount of water adsorption due to hydrophilic functional groups, and interactions between charge-carrying ions with charged functional groups (*i.e.* deprotonated AO groups).

To gain direct experimental evidence of the interactions of water and ions with polymer membranes at a molecular level, *in situ* solid-state nuclear magnetic resonance (ssNMR) spectroscopy was used to investigate AO-PIMs membranes with hydrophilicity tuned by degree of conversion (0% to 100 %). Two distinct peaks can be identified in the ^1H NMR spectra after the polymers are exposed to 20 wt% 1 M NaOH/ H_2O solution: one centred at 3 ppm and the other at 4 ppm, both of which move towards higher chemical shifts on increasing membrane hydrophilicity (Fig. 2g and Extended Data Fig. 6). Time-resolved ^1H and ^{23}Na spectra (Fig. 2h, Extended Data Fig. 6 and Supplementary Information Section 3.1.2.) reveal that water adsorption and the associated sodium ion diffusion into the pores occurs faster with higher AO modification. At only 32% conversion (Fig. 2i-j), the dynamic adsorption of water molecules and Na^+ ions into the membrane channels and wetting of channel walls were captured in real time, whereas at 56% and 100%, these processes were complete before data acquisition. These unprecedented real-time experimental observations of water and ion uptake in intrinsically microporous membranes suggest that water adsorption in the confined three-dimensional interconnected micropores leads to the formation of water-facilitated ionic channels, enabling fast transport of water and ions.

Selective ionic and molecular transport

Fast and selective ion transport in PIM membranes was demonstrated using concentration-driven dialysis diffusion tests (Fig. S19-20, Table S5-6). Free standing 300-nm-thick PIM-EA-TB membranes show a high permeation rate of hydrated K^+ ions of up to $10.8 \text{ mol m}^{-2} \text{ h}^{-1}$, much higher than that of low-

porosity DMBP-TB ($0.2 \text{ mol m}^{-2} \text{ h}^{-1}$) of the same thickness (Fig. 3a) and surpassing values of recently reported ionic-sieving membranes including graphene oxide membranes^{2, 27}. TB-PIM membranes show a sharp size-exclusion cut-off of $\sim 8.0 \text{ \AA}$, allowing the transport of smaller hydrated ions (K^+ , Na^+ , Li^+ , Cl^-) while rejecting larger ions such as hydrated Mg^{2+} (8.56 \AA). The ideal selectivity of K^+ over Mg^{2+} is up to 30-40 for PIM-BzMA-TB and untreated AO-PIM-1 membranes. High selectivity is also observed for binary salt dialysis (Fig. 3b and Table S6), demonstrating the potential of these PIM membranes in ion separation applications. Similarly, the PIM-BzMA-TB membrane also shows a high ideal $\text{Li}^+/\text{Mg}^{2+}$ selectivity of 33, despite the small difference in hydrated diameter (7.6 and 8.56 \AA). Contra-dialysis diffusion tests with equal concentration of anion (*i.e.*, Cl^-) on the feed and permeate sides (Fig. S20) confirmed the fast cation permeation and high selectivity. Ion transport in polymeric membranes is usually governed by the combination of Donnan exclusion, dielectric exclusion and steric hindrance (size-exclusion)⁴³. Since the three TB-PIM polymers contain the same TB functional groups with similar charge properties, the high selectivity of monovalent ions over divalent ions suggests that a size-exclusion mechanism dominates resulting from narrow ionic channels. Fast ion permeation rates and high selectivity result in the performance of PIM membranes surpassing those of existing nanofiltration membranes and graphene oxide and MXene-based ion-sieving membranes^{2, 28, 46-48} (Fig. 3b). The relative permeation rates of K^+ ions over the larger $\text{Fe}(\text{CN})_6^{3-}$ anions ($\sim 9.5 \text{ \AA}$), through both PIM-EA-TB and AO-PIM-1 show good selectivity of 48 and 82, respectively, comparable to that of Nafion (Fig. S19, Table S6). Hence these hydrophilic PIM membranes have potential for a range of applications such as ion separation, wastewater treatment, lithium ion extraction and recycling, and removal of heavy metal ions.

The size-selectivity was also demonstrated for recently reported redox active molecules with molecular weights in the range of 140-800 Da: 2,5-dihydroxy-1,4-benzoquinone (DHBQ)⁴⁹, 2,6-dihydroxyanthraquinone (2,6-DHAQ)¹⁰, $\text{K}_4\text{Fe}(\text{CN})_6$, riboflavin 5'-phosphate sodium salt (FMN-Na)¹³, and flavin adenine dinucleotide disodium salt hydrate (FAD). Nanofiltration studies in neutral-pH aqueous solutions showed that the PIM-EA-TB membrane achieved nearly 100% rejection of these molecules with the exception of the relatively small DHBQ (Fig. 3c, Fig. S21-23). Dialysis diffusion experiments confirmed that the crossover of these redox molecules through PIM membranes is generally very slow over 100 h in alkaline solutions (Fig. 3d, S24, Extended Data Fig. 7, and Table S7). Importantly, the permeance

of $\text{K}_4\text{Fe}(\text{CN})_6$ through AO-PIM-1 ($1.13 \times 10^{-3} \text{ mol m}^{-2} \text{ h}^{-1}$) and AO-PIM-SBF ($3.41 \times 10^{-5} \text{ mol m}^{-2} \text{ h}^{-1}$), is at least an order of magnitude lower than that of commercial Nafion 212 ($1.17 \times 10^{-2} \text{ mol m}^{-2} \text{ h}^{-1}$). In addition, the diffusion of redox-active organic molecules including DHAQ and FMN are generally slower than that of $\text{K}_4\text{Fe}(\text{CN})_6$. Furthermore, in contra-diffusion crossover tests, the permeance of $\text{K}_4\text{Fe}(\text{CN})_6$ through AO-PIM-1 dropped from $1.13 \times 10^{-3} \text{ mol m}^{-2} \text{ h}^{-1}$ to around $1.5 \times 10^{-4} \text{ mol m}^{-2} \text{ h}^{-1}$, which is much lower than that of commercial Nafion 212 membranes ($5.91 \times 10^{-3} \text{ mol m}^{-2} \text{ h}^{-1}$) (Extended Data Fig. 7 and Table S8). Since these crossover tests were performed using alkaline solution, in which both the organic redox molecules and AO-PIM-1 membranes are negatively charged, charge exclusion may also contribute to the low crossover rates. Overall, these results confirm that PIM membranes effectively block large redox active molecules while enabling fast ion transport, which is crucial for the operation of organic RFBs.

Ion-selective PIM membranes for efficient and stable aqueous redox flow batteries

The hydrophilic PIM membranes were incorporated into aqueous redox flow batteries using recently reported organic redox couples (Fig. S25, Table S10), including DHBQ| $\text{K}_4\text{Fe}(\text{CN})_6$ ⁴⁹(Fig. S28), FMN-Na| $\text{K}_4\text{Fe}(\text{CN})_6$ ¹³(Extended Data Fig. 8), and 2,6-DHAQ| $\text{K}_4\text{Fe}(\text{CN})_6$ ¹⁰ (Extended Data Fig. 9) for which the cyclic voltammetry curves are shown in Fig. 4b. EIS was used to investigate the area-specific resistance of TB-based and AO-functionalized PIM membranes (Fig. 4c, f, and Table S9). Crossover tests suggest that FMN-Na achieves near-100% rejection for all PIM membranes (Fig. 3d, Extended Data Fig. 7I). Therefore, the FMN-Na| $\text{K}_4\text{Fe}(\text{CN})_6$ redox couple was used to determine the influence of the membrane area-specific resistance on battery performance. Microporous PIM-EA-TB and PIM-BzMA-TB were easily fabricated into nanoscale films, resulting in a significantly optimised area-specific resistance of 1.20 and 1.60 $\Omega \text{ cm}^2$, respectively, lower than that of the less porous DMBP-TB (10.7 $\Omega \text{ cm}^2$). Similarly, AO-PIM-1 membranes with the proportion of AO groups at 56, 63 and 100% have area-specific resistances of 10.4, 2.90 and 1.04 $\Omega \text{ cm}^2$, respectively. The high-frequency area specific resistance of AO-PIM-1 measured in a flow cell is about 0.75 $\Omega \text{ cm}^2$ at 50% SOC, which is approximate to 0.97 $\Omega \text{ cm}^2$ at 0% SOC (Fig. S27). The slight decrease in ASR at higher SOC may be due to membrane activation during the charging process. Redox flow batteries assembled from membranes with lower resistance generally show a lower voltage gap in polarization tests (Fig. 4d, 4g), yielding a higher power density (Fig. S26) and higher energy efficiency

(Fig. 4e, 4h). These results suggest that the hydrophilic ionizable groups in AO-PIMs play an important role in reducing ion transport resistance and achieving the efficient operation of RFBs.

A RFB based on the small quinone redox molecule DHBQ⁴⁹ paired with K₄Fe(CN)₆, showed a swift battery capacity decay from 2.3 to 1.4 Ah l⁻¹ over the initial 10 cycles (Fig. S28), consistent with rapid DHBQ crossover (Fig. 3c). In contrast, RFBs assembled with a redox couple of FMN-Na|K₄Fe(CN)₆ using either a PIM-EA-TB thin film composite or an AO-PIM-1 membrane showed high cycling stability with electrochemical capacity retention of 86.5% and 84.5%, respectively, over 200 cycles at 80 mA cm⁻² (Fig. 4i, Extended Data Fig. 8). These values are comparable to that obtained from the equivalent RFB with a Nafion 212 membrane (85.1%). The area-specific resistance and conductivities of AO-PIM-1 in alkaline solution were unchanged during cycling (Fig. S29). Therefore, the slow decay of discharge capacity in these FMN-Na-based RFBs can be attributed to the known instability¹² of FMN in strong alkaline solution¹². Further experiments confirmed that degradation of FMN-Na leads to battery capacity decay (Fig. S30). RFBs based on the 2,6-DHAQ|K₄Fe(CN)₆ redox couple operated in an argon-filled glovebox (Fig. 4j) achieved high coulombic efficiencies of >99.8 % with both PIM-EA-TB and AO-PIM-1 membranes at 40 mA cm⁻². The RFB using an AO-PIM-1 membrane exhibited the lowest capacity fade rate of 0.5% per day (0.006% per cycle), which is superior to the performance of Nafion 212 membrane (2.3% per day, 0.025% per cycle) (Fig. 4j and Extended Data Fig. 10). The crossover rate of iron-containing species through AO-PIM-1 in an operating RFB was quantitatively determined by *ex-situ* ICP-OES to be 1.48×10⁻⁴ mol m⁻² h⁻¹, which is significantly lower than that of an identical RFB using a Nafion 212 membrane (6.37×10⁻⁴ mol m⁻² h⁻¹) (Fig. 3d and inset in Fig. 4j, Extended Data Fig. 10, and Fig. S32). Much more rapid decay of performance was observed by operating the 2,6-DHAQ-K₄Fe(CN)₆ battery in the open-air rather than an argon atmosphere (Fig. S31) suggests that oxygen causes degradation of the redox compounds. Although further work is required to fully understand the battery decay based on the degradation and crossover of organic molecules, it is clear that the highly conductive and selective PIM membranes enable the battery to perform with significantly enhanced stability (Supplementary Information Section 4.4.). Indeed, based on the crossover of redox active species (*e.g.* K₄Fe(CN)₆), if we assume that the battery performs only one cycle per day with charging-discharging duration of 4 h, and the electrolytes are isolated from the membrane during the 20 hours when the battery isn't operating, we estimate that the lifetime of an RFB based on AO-

PIM-1 (~6300 days) will be longer than that of a similar RFB based on Nafion 212 (~1464 days) (Table S11-12, and Supplementary Information Section 4.4.4).

Outlook

The concept of generating intrinsic microporosity within solution processable polymers, via chain rigidity and contortion, combined with the incorporation of hydrophilic functional groups to optimise hydrophilicity and ion-conductivity has resulted in a new generation of ion selective membranes. For the fabrication of RFBs, these membranes show low area-specific resistance, fast ion permeation rate, and unprecedented selectivity towards redox couples, leading to RFB performance and stability that is comparable, and in some cases superior, to those based on benchmark Nafion membranes. PIMs, whose structural diversity can be controlled by monomer choice, polymerisation reaction and post-synthetic modification, allow for the rational optimisation of membranes for RFBs based on a wide variety of redox chemistries. For example, the more porous AO-PIM-SBF provided a membrane with enhanced ionic conductivity relative to AO-PIM-1 and our current effort is directed towards improving this polymer's robustness so as maintain its improved RFB performance. The modification of ultrapermeable PIMs with even greater intrinsic microporosity, such as those based on benzotriptycene⁵⁰, may increase ionic conductivity further. Importantly, thin-film composite membranes can be prepared using roll-to-roll technology and low-cost supports. Hence, these innovative membranes could be cost-effective and applicable to a wide range of energy-related devices including fuel cells, redox flow batteries and electrochemical reactors in addition to water treatment processes such as electrodialysis, nanofiltration and desalination.

References

1. Werber, J.R., Osuji, C.O. & Elimelech, M. Materials for next-generation desalination and water purification membranes. *Nature Reviews Materials* **1**, 16018 (2016).
2. Joshi, R.K. et al. Precise and Ultrafast Molecular Sieving Through Graphene Oxide Membranes. *Science* **343**, 752-754 (2014).
3. Park, M., Ryu, J., Wang, W. & Cho, J. Material design and engineering of next-generation flow-battery technologies. *Nature Reviews Materials* **2**, 16080 (2016).
4. Turner, J.A. Sustainable Hydrogen Production. *Science* **305**, 972-974 (2004).
5. Park, C.H. et al. Nanocrack-regulated self-humidifying membranes. *Nature* **532**, 480 (2016).
6. Li, C.W., Ciston, J. & Kanan, M.W. Electroreduction of carbon monoxide to liquid fuel on oxide-derived nanocrystalline copper. *Nature* **508**, 504 (2014).
7. Soloveichik, G.L. Flow Batteries: Current Status and Trends. *Chemical Reviews* **115**, 11533-11558 (2015).
8. Huskinson, B. et al. A metal-free organic-inorganic aqueous flow battery. *Nature* **505**, 195 (2014).
9. Janoschka, T. et al. An aqueous, polymer-based redox-flow battery using non-corrosive, safe, and low-cost materials. *Nature* **527**, 78 (2015).

10. Lin, K. et al. Alkaline quinone flow battery. *Science* **349**, 1529 (2015).
11. Hollas, A. et al. A biomimetic high-capacity phenazine-based anolyte for aqueous organic redox flow batteries. *Nature Energy* **3**, 508-514 (2018).
12. Lin, K. et al. A redox-flow battery with an alloxazine-based organic electrolyte. *Nature Energy* **1**, 16102 (2016).
13. Orita, A., Verde, M.G., Sakai, M. & Meng, Y.S. A biomimetic redox flow battery based on flavin mononucleotide. *Nature Communications* **7**, 13230 (2016).
14. Kwabi, D.G. et al. Alkaline Quinone Flow Battery with Long Lifetime at pH 12. *Joule* **2**, 1894–1906 (2018).
15. Shin, D.W., Guiver, M.D. & Lee, Y.M. Hydrocarbon-Based Polymer Electrolyte Membranes: Importance of Morphology on Ion Transport and Membrane Stability. *Chemical Reviews* **117**, 4759-4805 (2017).
16. Li, B. & Liu, J. Progress and directions in low-cost redox-flow batteries for large-scale energy storage. *National Science Review* **4**, 91-105 (2017).
17. Darling, R.M., Gallagher, K.G., Kowalski, J.A., Ha, S. & Brushett, F.R. Pathways to low-cost electrochemical energy storage: a comparison of aqueous and nonaqueous flow batteries. *Energy & Environmental Science* **7**, 3459-3477 (2014).
18. Grey, C.P. & Tarascon, J.M. Sustainability and in situ monitoring in battery development. *Nature Materials* **16**, 45 (2016).
19. Park, C.H., Lee, C.H., Guiver, M.D. & Lee, Y.M. Sulfonated hydrocarbon membranes for medium-temperature and low-humidity proton exchange membrane fuel cells (PEMFCs). *Prog. Polym. Sci.* **36**, 1443-1498 (2011).
20. Trigg, E.B. et al. Self-assembled highly ordered acid layers in precisely sulfonated polyethylene produce efficient proton transport. *Nature Materials* **17**, 725-731 (2018).
21. Yuan, Z. et al. Advanced porous membranes with ultra-high selectivity and stability for vanadium flow batteries. *Energy & Environmental Science* **9**, 441-447 (2016).
22. Pezeshki, A.M. et al. Full Cell Study of Diels Alder Poly(phenylene) Anion and Cation Exchange Membranes in Vanadium Redox Flow Batteries. *J. Electrochem. Soc.* **163**, A5154-A5162 (2016).
23. Sun, C.-N., Tang, Z., Belcher, C., Zawodzinski, T.A. & Fujimoto, C. Evaluation of Diels–Alder poly(phenylene) anion exchange membranes in all-vanadium redox flow batteries. *Electrochemistry Communications* **43**, 63-66 (2014).
24. Sorte, E.G. et al. Impact of Hydration and Sulfonation on the Morphology and Ionic Conductivity of Sulfonated Poly(phenylene) Proton Exchange Membranes. *Macromolecules* **52**, 857-876 (2019).
25. Maurya, S. et al. Rational design of polyaromatic ionomers for alkaline membrane fuel cells with >1 W cm⁻² power density. *Energy & Environmental Science* **11**, 3283-3291 (2018).
26. Lee, K.-S., Spendlow, J.S., Choe, Y.-K., Fujimoto, C. & Kim, Y.S. An operationally flexible fuel cell based on quaternary ammonium-biphosphate ion pairs. *Nature Energy* **1**, 16120 (2016).
27. Chen, L. et al. Ion sieving in graphene oxide membranes via cationic control of interlayer spacing. *Nature* **550**, 380 (2017).
28. Abraham, J. et al. Tunable sieving of ions using graphene oxide membranes. *Nature Nanotechnology* **12**, 546 (2017).
29. Huang, N., Wang, P. & Jiang, D. Covalent organic frameworks: a materials platform for structural and functional designs. *Nature Reviews Materials* **1**, 16068 (2016).
30. Xu, H., Tao, S. & Jiang, D. Proton conduction in crystalline and porous covalent organic frameworks. *Nature Materials* **15**, 722 (2016).
31. Bai, S., Liu, X., Zhu, K., Wu, S. & Zhou, H. Metal–organic framework-based separator for lithium–sulfur batteries. *Nature Energy* **1**, 16094 (2016).
32. Zhang, H. et al. Ultrafast selective transport of alkali metal ions in metal organic frameworks with subnanometer pores. *Science Advances* **4**, eaaq0066 (2018).
33. Furukawa, H., Cordova, K.E., O’Keeffe, M. & Yaghi, O.M. The Chemistry and Applications of Metal–Organic Frameworks. *Science* **341**, 1230444 (2013).
34. Li, C. et al. Polysulfide-Blocking Microporous Polymer Membrane Tailored for Hybrid Li-Sulfur Flow Batteries. *Nano Letters* **15**, 5724-5729 (2015).
35. Chae, I.S. et al. Ultra-High Proton/Vanadium Selectivity for Hydrophobic Polymer Membranes with Intrinsic Nanopores for Redox Flow Battery. *Advanced Energy Materials* **6**, 1600517 (2016).
36. Budd, P.M. et al. Solution-Processed, Organophilic Membrane Derived from a Polymer of Intrinsic Microporosity. *Advanced Materials* **16**, 456-459 (2004).
37. McKeown, N.B. & Budd, P.M. Polymers of intrinsic microporosity (PIMs): organic materials for membrane separations, heterogeneous catalysis and hydrogen storage. *Chemical Society Reviews* **35**, 675-683 (2006).
38. Carta, M. et al. An Efficient Polymer Molecular Sieve for Membrane Gas Separations. *Science* **339**, 303 (2013).

39. Patel, H.A. & Yavuz, C.T. Noninvasive functionalization of polymers of intrinsic microporosity for enhanced CO₂ capture. *Chemical Communications* **48**, 9989-9991 (2012).
40. Bezzu, C.G. et al. The synthesis, chain-packing simulation and long-term gas permeability of highly selective spirobifluorene-based polymers of intrinsic microporosity. *Journal of Materials Chemistry A* **6**, 10507-10514 (2018).
41. Bezzu, C.G. et al. A Spirobifluorene-Based Polymer of Intrinsic Microporosity with Improved Performance for Gas Separation. *Advanced Materials* **24**, 5930-5933 (2012).
42. Swaidan, R., Ghanem, B.S., Litwiller, E. & Pinnau, I. Pure- and mixed-gas CO₂/CH₄ separation properties of PIM-1 and an amidoxime-functionalized PIM-1. *Journal of Membrane Science* **457**, 95-102 (2014).
43. Geise, G.M., Paul, D.R. & Freeman, B.D. Fundamental water and salt transport properties of polymeric materials. *Prog. Polym. Sci.* **39**, 1-42 (2014).
44. Schmidt-Rohr, K. & Chen, Q. Parallel cylindrical water nanochannels in Nafion fuel-cell membranes. *Nature Materials* **7**, 75 (2007).
45. Mehio, N. et al. Acidity of the Amidoxime Functional Group in Aqueous Solution: A Combined Experimental and Computational Study. *The Journal of Physical Chemistry B* **119**, 3567-3576 (2015).
46. Hatakeyama, E.S. et al. Water filtration performance of a lyotropic liquid crystal polymer membrane with uniform, sub-1-nm pores. *Journal of Membrane Science* **366**, 62-72 (2011).
47. Wen, Q. et al. Highly Selective Ionic Transport through Subnanometer Pores in Polymer Films. *Adv. Funct. Mater.* **26**, 5796-5803 (2016).
48. Ren, C.E. et al. Charge- and Size-Selective Ion Sieving Through Ti₃C₂T_x MXene Membranes. *The Journal of Physical Chemistry Letters* **6**, 4026-4031 (2015).
49. Yang, Z. et al. Alkaline Benzoquinone Aqueous Flow Battery for Large-Scale Storage of Electrical Energy. *Advanced Energy Materials* **8**, 1702056 (2018).
50. Rose, I. et al. Polymer ultrapermeability from the inefficient packing of 2D chains. *Nature Materials* **16**, 932 (2017).

Acknowledgement

This work was funded by the Engineering and Physical Sciences Research Council (EPSRC, UK, EP/M01486X/1), EPSRC Centre for Advanced Materials for Integrated Energy Systems (CAM-IES, EP/P007767/1), the Horizon 2020/FP7 Framework Program under grant agreement no. 608490, project M⁴CO₂, and the European Research Council through grant agreement number 758370 (ERC-StG-PE5- CoMMaD). Q.S. acknowledges the financial support by Imperial College Department of Chemical Engineering Start-up Fund, seed-funding grant from Institute of Molecular Science and Engineering (IMSE, Imperial College) and seed-funding from EPSRC centres CAM-IES and Energy SuperStore (UK Energy Storage Research Hub). R.T. acknowledges a full PhD scholarship funded by China Scholarship Council. A.W. acknowledges a full PhD scholarship funded by Department of Chemical Engineering at Imperial College. B.P.D. acknowledges the Statoil scholarship. K.E.J. acknowledge the Royal Society University Research Fellowship. A.I.C. and L.C. acknowledge the Leverhulme Trust for supporting the Leverhulme Research Centre for Functional Materials Design. T. Li is thankful for the support from the Joint Center for Energy Storage Research (JCESR), a U.S. Department of Energy, Energy Innovation Hub. The work at the APS was supported by the US Department of Energy Scientific User Facilities under Contract DEAC02-06CH11357 with UChicago Argonne, LLC, and operator of Argonne National Laboratory. The authors acknowledge E. Hunter-Sellers and Prof. D. Williams for facility support for DVS measurements and Prof. A.G. Livingston for facility support for manufacturing polyacrylonitrile membranes. The authors acknowledge Dr. R. Woodward and Dr. R. Rinaldi for help with GPC measurements. The authors thank V. Yufit for helpful discussion. The authors acknowledge Q. Zhang, Y. Liu, S. Zhang, and T. Juergensen for assistance with membrane preparation and battery tests.

Contributions

Q.S., R.T., and A.W. developed membranes and redox flow batteries. A.W. synthesised PIM-1, AO-PIMs, Amine-PIM-1 and DMBP-TB polymers, prepared membranes and performed characterizations. R.M. synthesized TB-PIMs and carried out characterizations. C.Y. synthesised PIM-SBF and performed modification and characterizations. R.T. and A.W. carried out the ion transport and diffusion measurements. X.Z. and Z.F. helped with the crossover measurements. R.T. and A.W. performed electrochemical and flow battery experiments. B.P.D. helped with membrane preparation, installation of the redox flow battery and electrochemical tests. E.Z., T. Liu, and C.P.G. contributed to solid state NMR measurements and interpretation and provided insights into the research. L.T., E. J., L.C., S.Y.C., K.E.J. and A.I.C. contributed to molecular simulations and analyses. T. Li contributed to the SAXS measurements. N.P.B. provided facility support and insights into flow battery systems. R.T., A.W., N.B.M. and Q.S. wrote the manuscript with contribution from all co-authors. All of the authors participated in the discussion and commented on the manuscript. Q.S. conceived the project, designed the research, and directed the project with N.B.M.

Competing interests

The authors declare no competing interests.

Correspondence and requests for materials should be addressed to N.B.M. or Q.S.

Figure Caption
Figure Caption

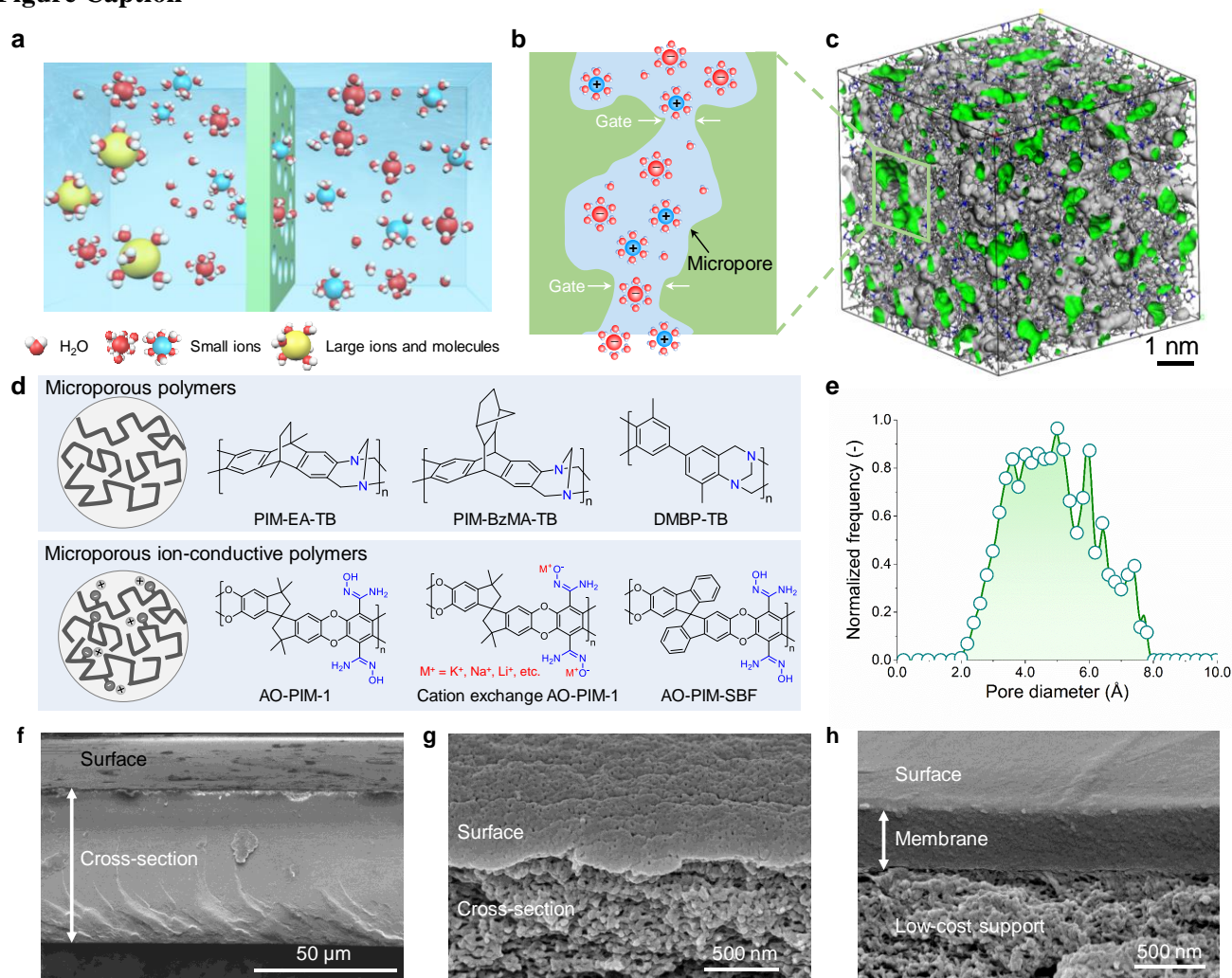


Figure 1 | Ion-selective microporous membranes. **a**, Working principle of hydrophilic microporous membranes for fast ion transport and high ionic and molecular selectivity. **b**, Schematic diagram of interconnected sub-nanometer-sized cavities in microporous membranes for rapid and selective ion transport. **c**, Three-dimensional view of an amorphous cell of PIM-EA-TB polymer. Cell size: 66.8×66.8×66.8 Å. The grey surface indicates the van der Waals surface, and green surface is the Connolly surface with probe radius of 1.55 Å. **d**, Macromolecular structures of microporous polymers with size-selective ion separation function, and typical structures of hydrophilic microporous PIM polymers including PIM-EA-TB, PIM-BzMA-TB, DMBP-TB. Inset diagram shows the inefficient packing of rigid and contorted polymer chains. Macromolecular structures of microporous polymers with both size-exclusion and ion-conductive functionality, including typical examples of amidoxime-functionalized PIM-1 (AO-PIM-1) and deprotonated cation-exchange AO-PIM-1 in alkaline solutions at high pH, and AO-PIM-SBF studied in this work. Inset schematic diagram shows the inefficient packing of rigid and contorted polymer chains with negative charged functional groups located on the rigid backbone that facilitate the transport of cations. **e**, Normalized pore size distribution derived from molecular simulation as shown in (c). **f**, Cross-sectional SEM image of an AO-PIM-1 membrane. **g**, Cross-sectional SEM image of a low-cost mesoporous polyacrylonitrile support membrane. **h**, Cross-sectional SEM image of a TFC membrane consisting of an ion-selective PIM polymer membrane (PIM-EA-TB) coated on the mesoporous polyacrylonitrile support.

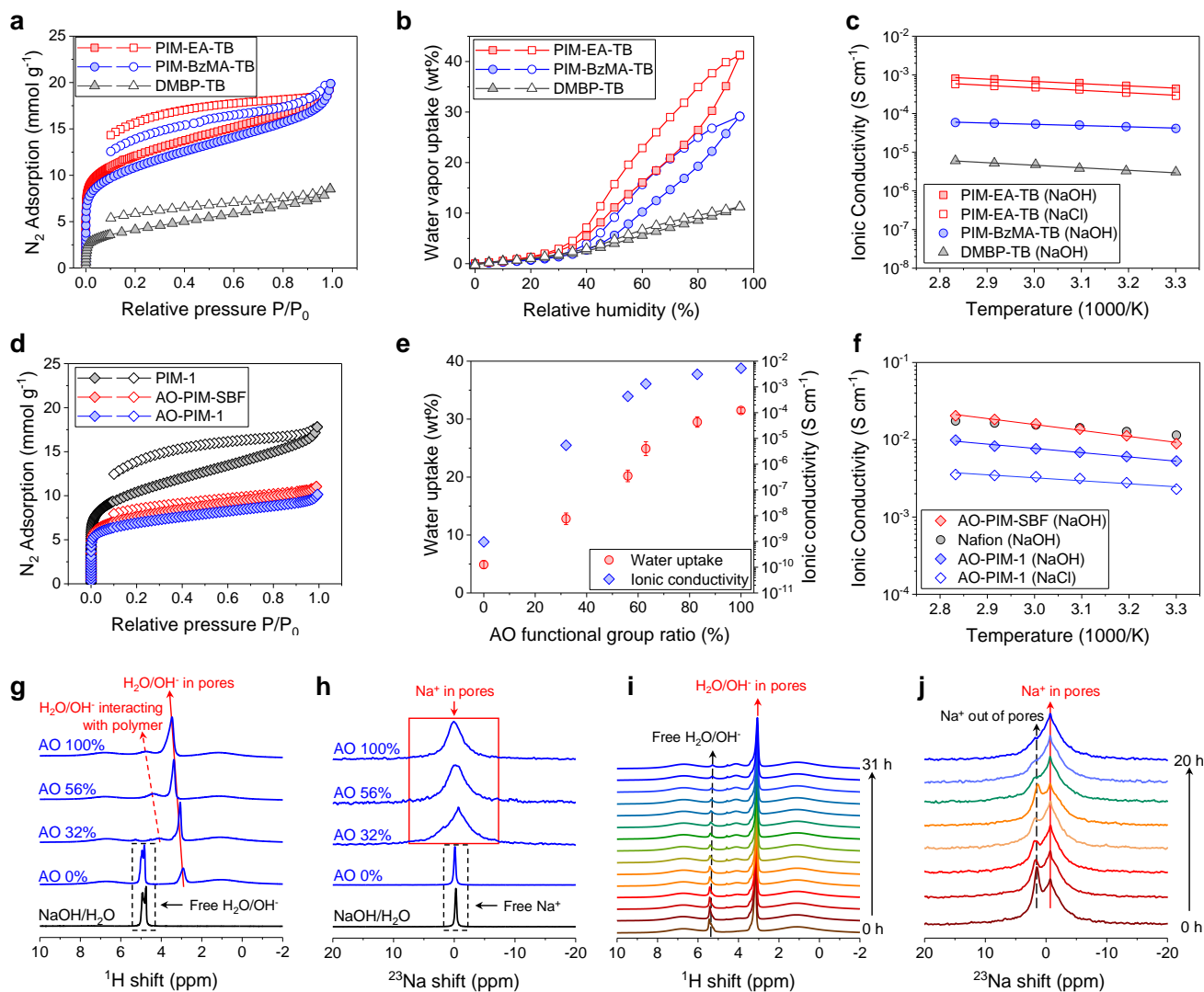


Figure 2 | Water adsorption, ionic conductivity and ionic dynamics of microporous membranes. **a**, N_2 adsorption–desorption isotherms of Tröger-base containing PIM polymers (TB-PIMs) at 77 K. **b**, Water vapor sorption isotherms of thick self-supported TB-PIM membranes at 25°C measured by DVS. **c**, Temperature dependence of ionic conductivities of thick self-supported TB-PIM membranes measured in 1 M NaOH (filled symbol) or 1 M NaCl (open symbol) by electrochemical impedance spectroscopy. **d**, N_2 adsorption-desorption isotherms of PIM-1, AO-PIM-1 and AO-PIM-SBF polymers at 77 K. symbols in **a**, **b**, and **d**: filled, adsorption; open, desorption. **e**, Bulk water uptake and ionic conductivity as a function of amidoxime functional group ratio (from 32% to 100%) in amidoxime-functionalized PIM-1 (AO-PIMs). Error bars are standard deviations using at least three measurements from different samples. Ionic conductivity was measured in 1 M NaOH at 30°C. **f**, Temperature dependence of ionic conductivities of AO-PIMs and Nafion 212 membranes measured in 1 M NaOH (filled symbol) or 1 M NaCl (open symbol) by electrochemical impedance spectroscopy. **g–j**, Water and ionic dynamics in microporous membranes probed by in situ solid-state NMR spectroscopy: **g**, Equilibrated ^1H solid state nuclear magnetic resonance (ssNMR) spectra and, **h**, ^{23}Na ssNMR of 1M NaOH in H_2O in AO-PIM membranes with varied portion of amidoxime groups (10 mg). **i**, Time-resolved ^1H ssNMR spectra showing the dynamic adsorption of $\text{H}_2\text{O}/\text{OH}^-$ in micropores of AO-PIM-1 membrane with 32% of amidoxime groups. **j**, Time-resolved ^{23}Na ssNMR spectra showing the dynamic adsorption of Na ions in micropores of AO-PIM-1 membrane with 32% of amidoxime groups.

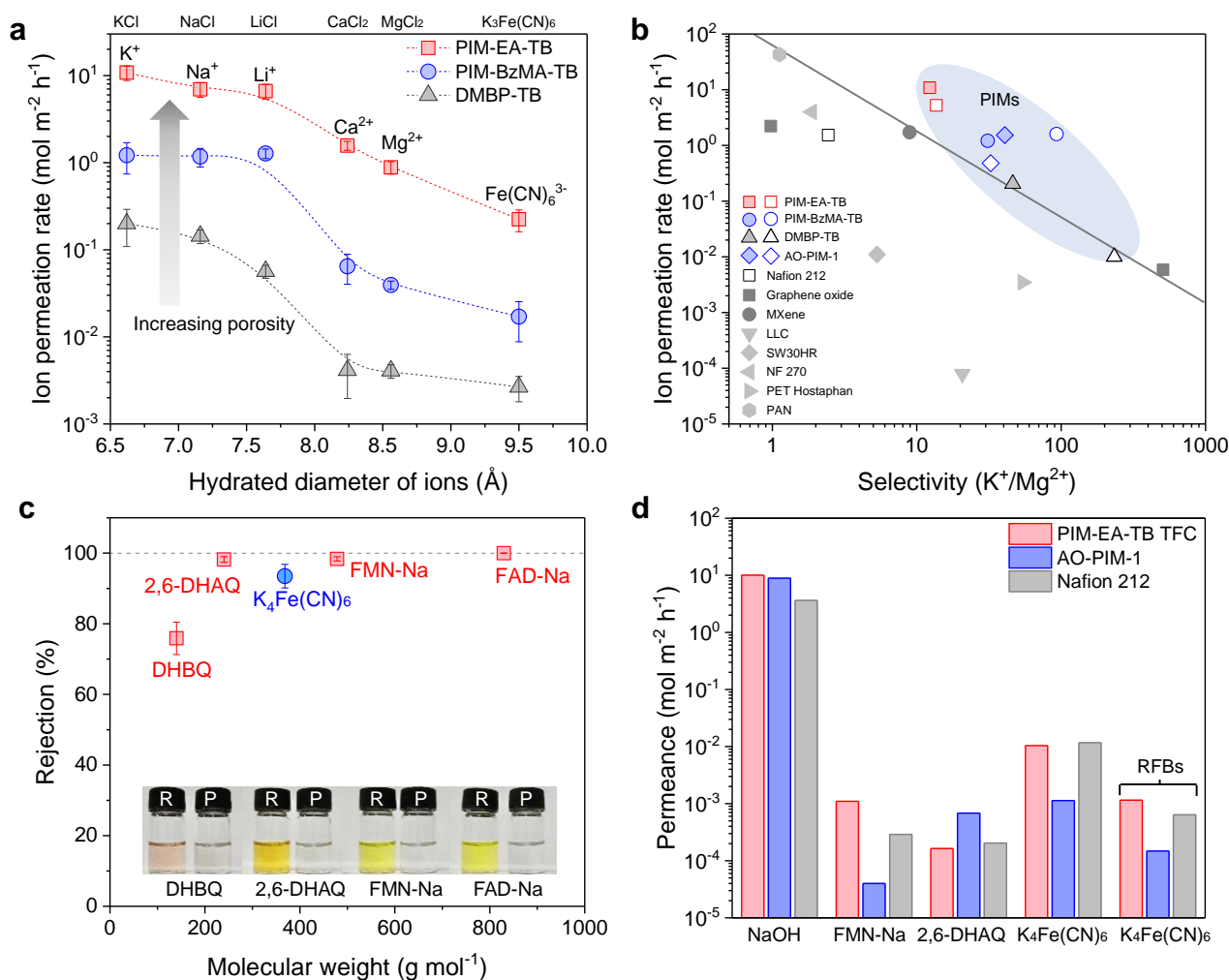


Figure 3 | Ionic and molecular sieving. **a**, Selective ion permeation of common salts through freestanding microporous PIM membranes with a thickness of about 300 nm. Dashed lines are added to guide the eyes. The feed solution: 1 M salt solution in high-purity deionized water, including KCl, NaCl, LiCl, CaCl_2 , MgCl_2 and $\text{K}_3\text{Fe}(\text{CN})_6$ with varied hydrated diameter of cations or anions^{2, 28}. The permeate side: high-purity deionized water. **b**, K^+ permeation rate versus $\text{K}^+/\text{Mg}^{2+}$ selectivity for PIMs membranes. Solid symbols: ideal selectivity; Open symbols: binary salt selectivity. Typical ion separation data of ion-exchange membrane, nanofiltration membranes, and state-of-the-art ion-sieving membranes such as graphene-oxide and MXene membranes reported in the literature^{2, 28, 46-48} are included. The line is added manually to show the trade-off between the ion permeation and selectivity towards large ions. **c**, Rejection of redox materials measured by nanofiltration using thin film composite membranes consisting a PIM-EA-TB thin film supported on a porous polyacrylonitrile substrate. Typical commercially available redox active materials with varied molecular size for redox flow batteries, including 2,5-dihydroxy-1,4-benzoquinone (DHBQ), 2,6-dihydroxyanthraquinone (2,6-DHAQ), $\text{K}_4\text{Fe}(\text{CN})_6$, riboflavin 5'-phosphate sodium salt (FMN-Na), and flavin adenine dinucleotide (FAD-Na). The feed aqueous solution (20 ppm) was pressurised in a nanofiltration stirred cell under a feed pressure of 10 bar at room temperature. Inset photo shows the colours of retentate (R) and permeate (P) solutions for typical redox molecules. Error bars are standard deviations using at least three measurements from different samples. **d**, Permeance of NaOH, FMN-Na, 2,6-DHAQ, $\text{K}_4\text{Fe}(\text{CN})_6$ through PIM-EA-TB TFC, AO-PIM-1 and Nafion 212 measured by single redox-specie /salt dialysis diffusion tests in H-cells and operating RFBs (labelled above the columns).

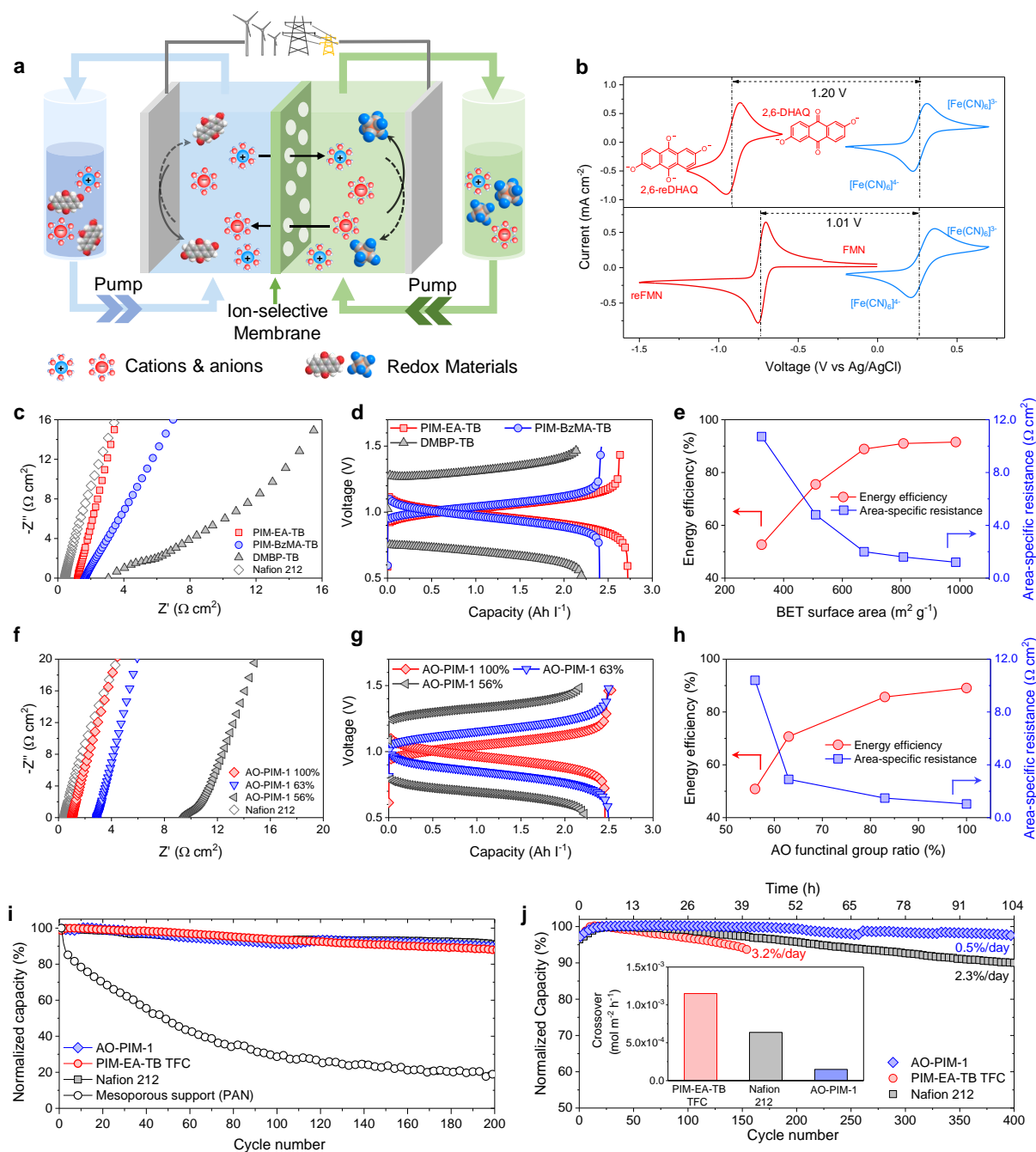


Figure 4 | Hydrophilic microporous membranes enable efficient and stable operation of aqueous redox flow batteries. **a**, Schematic diagram of a redox flow battery system for grid scale energy storage. Redox materials are visualized using the 3D molecular models of 2,6-DHAQ and $\text{Fe}(\text{CN})_6$ couple. **b**, Cyclic voltammogram of 2mM 2,6-DHAQ, FMN-Na (red curve) and ferrocyanide (blue curve) at a scanning rate of 10 mV/s on glassy carbon electrode. The theoretical potentials were marked in this figure. **c**, EIS spectra of TB-PIM membranes and Nafion 212 in 1 M NaOH. **d**, Voltage versus capacity for TB-PIM membranes with FMN-Na (0.1 M) | $\text{K}_4\text{Fe}(\text{CN})_6$ (0.1 M) redox couple in 1M NaOH solution at a charging-discharging rate of 20 mA cm^{-2} . **e**, Battery energy efficiency and membrane area-specific resistance versus the BET surface areas of TB-PIM polymers. PIM-BzMA-TB and DMBP-TB were blended at a certain ratio (*i.e.*, 1:2 and 2:1 by weight) to yield blend polymers with the BET surface area of 509 and 674 $\text{m}^2 \text{g}^{-1}$, respectively, as measured by N_2 adsorption. **f**, EIS spectra of Nafion 212 and AO-PIM-1 membranes with a varied proportion of AO groups in 1 M NaOH. **g**, Voltage versus capacity for AO-PIM-1 membranes with FMN-Na(0.1 M) | $\text{K}_4\text{Fe}(\text{CN})_6$ (0.1 M) redox couple in 1M NaOH solution at a charging-discharging rate of 20 mA cm^{-2} . **h**, Battery energy efficiency and membrane area-specific resistance versus conversion degree of AO functional groups. Lines in (e) and (h) are added to guide the eyes. **i**, Cycling stability of FMN-Na| $\text{K}_4\text{Fe}(\text{CN})_6$ battery assembled with PIM-EA-TB TFC, AO-PIM-1 and Nafion 212 membranes. Mesoporous PAN membrane is included for comparison. **j**, Cycling performance of RFBs assembled with PIM-EA-TB TFC, AO-PIM-1 and Nafion 212 membranes in an Argon-filled glove box with 2,6-DHAQ | $\text{K}_4\text{Fe}(\text{CN})_6$ redox couple in 1M NaOH solution under a current density of 40 mA cm^{-2} . To evaluate cycling stability, discharge capacity is normalized by the fully-discharged capacity. Inset figure shows the crossover rates of iron-containing species through membranes in the operating batteries.

Methods

Materials. Most of chemicals were commercially purchased from Sigma-Aldrich and TCI without further purification, including potassium ferrocyanide ($K_4Fe(CN)_6$, >99%), sodium ferrocyanide ($Na_4Fe(CN)_6$, >99%), riboflavin-5'-phosphate sodium salt (FMN-Na, >93%), flavin adenine dinucleotide disodium salt hydrate (FAD-Na, >95%), 2,6-dihydroxy-anthraquinone (2,6-DHAQ, >90%), 2,5-Dihydroxy-1,4-benzoquinone (DHBQ, >98%), anhydrous zinc chloride ($ZnCl_2$, >99%), anhydrous potassium chloride (KCl, >99%), anhydrous sodium chloride (NaCl, >99%), anhydrous lithium chloride (>98%), anhydrous calcium chloride ($CaCl_2$, >97%), anhydrous magnesium chloride ($MgCl_2$, >98%), potassium hexacyanoferrate ($K_3Fe(CN)_6$, >99%), potassium hydroxide (anhydrous, >99%), sodium hydroxide (NaOH, >99%), and superconductive carbon (KJ-black).

Membranes and substrates: Nafion[®]212 (Dupont) membranes were purchased from Sigma-Aldrich. PTFE substrates were purchased from Cole-Parmer.

Synthesis of PIM-1. PIM-1 polymer was synthesised following the published method⁵¹. 3,3,3',3'-tetramethyl-1,1'-spirobisindane-5,5',6,6'-tetrol (TTSBI) was purified by recrystallization in methanol/dichloromethane. 2,3,5,6-tetrafluoroterephthalonitrile (TFTPN) was purified by recrystallization in methanol, followed by vacuum sublimation at 155°C. Purified monomers TTSBI (10.21 g, 30 mmol) and TFTPN (6.00 g, 30 mmol) were dissolved in anhydrous DMF (200 ml). Anhydrous K_2CO_3 (8.40g, 60.8 mmol) was added to this solution and the mixture was heated to 70°C for 72 h under N_2 . The reaction mixture was poured into 1 L water and the solid collected by filtration then washed with water, acetone and methanol. The polymer was purified by repeated precipitation from chloroform solution by adding methanol drop-wise until the solution became turbid. The purified polymer was collected by filtration and dried at 110°C under vacuum to yield yellow powders.

Synthesis of AO-PIM-1 and AO-PIM-SBF. AO-PIM-1 was synthesised by modifying PIM-1 polymer following a published protocol³⁹. PIM-1 (4.80 g) was dissolved in THF (300 ml) and heated to 65°C. To this, hydroxylamine solution (50 ml, 50 wt.% in H_2O) was added dropwise and the mixture was allowed to reflux for 20 h under N_2 . The reaction mixture was poured into 1 L ethanol and the solid collected by filtration then washed with ethanol. The product was dried at 100°C under vacuum to yield off-white powders. AO-PIM-1 with varied contents of amidoxime functionality (32%, 56%, 63% and 83% as confirmed by ssNMR) were obtained by shortening the reaction time to 30 min, 1 h, 2.5 h and 5 h, respectively. For simplicity, fully converted AO-PIM-1 was named as AO-PIM-1, while partially converted AO-PIM-1 polymers with varied degree of AO groups were named as AO-PIM-1 32%, AO-PIM-1 56%, AO-PIM-1 63% and AO-PIM-1 83%. AO-PIM-SBF with 100% conversion of nitrile group was prepared similarly from PIM-SBF^{40, 41}.

Synthesis of Tröger's base PIM polymers. Tröger's base PIM polymers were synthesised following a previously reported method, including PIM-EA-TB, PIM-BzMA-TB and DMBP-TB⁵². Detailed synthetic methods of monomers for PIM-BzMA-TB are given in the Supplementary information. In general, a certain aromatic diamine monomer (1 mol eq.) was dissolved in dimethoxymethane (5 mol eq.) under nitrogen and the solution cooled to 0 °C. To this, trifluoroacetic acid (120 mol eq.) was added dropwise over 30 min and the solution was stirred for an appropriate time at room temperature. The viscous reaction solution was slowly poured into aqueous ammonium hydroxide solution and the mixture stirred vigorously for 2 h during which time an off-white solid was formed. The solid was filtered, washed with water and then acetone until the washings were clear. The polymer was purified by repeated precipitation from chloroform solution by adding methanol drop-wise until the solution became turbid. The purified polymer was collected by filtration and dried at 110°C under vacuum to polymer powders. In some cases, PIM-BzMA-TB and DMBP-TB were blended to achieve polymer samples with tuned surface area and free volume. The two polymers were dissolved in chloroform with certain weight ratio to form a homogeneous solution, and then precipitated in hexane, and further dried at 110°C under vacuum before adsorption analysis.

Fabrication of membranes. Thick symmetric membranes were fabricated by casting polymer solutions on clean glass plates using a doctor blade. Chloroform, THF or DMF was used as the solvent to prepare polymer solutions depending on the solubility of PIMs (chloroform for PIM-1 and TB-based PIMs, THF for AO-PIM-1 32%, and DMF for AO-PIM-1 56%, 63%, 83% and 100%, respectively); polymer solutions were centrifuged at 12000 rpm for 5 mins to remove undissolved impurities. After blade casting, the polymer solution films were kept in a desiccator for two days at a certain temperature (room temperature for chloroform and THF and 60°C for DMF) in order for slow evaporation of the solvent. Dry polymer membranes were then peeled off from the glass plates and soaked in methanol overnight. Afterwards, the membranes were dried in air for 12 h and annealed at 110°C for another 12 h. The thickness of symmetric membranes was controlled by varying the gap thickness of doctor blade and the concentration of polymer dope solutions.

Thin films were fabricated by spin coating dilute polymer solutions onto a substrate.⁵³ Polymer solutions were filtered through syringe filters (PTFE, 0.45 μm) and dropped onto the substrate which was kept static. Then the substrate was rotated at a speed of 2000 rpm with an acceleration speed of 1500 rpm for 1 min. Thin film composite (TFC) membranes were prepared by using porous hydrophilic polytetrafluoroethylene (PTFE) membranes, porous anodized aluminum oxide (AAO) membranes, or porous polyacrylonitrile (PAN) ultrafiltration membranes prepared following previous protocol⁵⁴ as the substrate. In some cases, polymer blend films were prepared from PIM-BzMA-TB and

DMBP-TB by mixing the two polymers at certain weight ratio. Free standing thin films were prepared by using glass plates as the substrate, followed by floating them off onto a water surface. The thickness of the thin film was controlled by varying the concentration of polymer solutions in the range of 1.0 - 4.0 wt%.

Characterization techniques. Scanning electron microscopy (SEM) was performed using a Hitachi S5500 microscope. Before testing, the membranes were manually fractured in liquid nitrogen and coated with a thin layer of Au/Pd. The surfaces and cross-sectional morphologies of membranes were observed. Infrared spectroscopy was performed on a Perkin-Elmer Spectrum 100 FTIR spectrometer with polymer membrane samples mounted on a zinc-selenium/diamond plate. Thermal analyses were performed using a NETZSCH STA 449 F5 Jupiter thermogravimetric analyser. Polymer samples were heated from room temperature to 900 °C under flowing nitrogen at a heating rate of 10°C min⁻¹. Tensile tests were carried out using a Lloyd-Ametek EZ50 Material Testing Machine at room temperature and a relative humidity of around 50% with a strain rate of 10% min⁻¹. Nanomechanical properties were determined using Atomic Force Microscopy (AFM, Asylum Instruments MFP-3D) with a dual frequency technique (AM-FM) and nanosensor probes (PPP-NCHR, tip radius < 7nm, nom. Spring constant 42 N m⁻¹). Probes were calibrated before use using the built-in 'Get-Real' software. Typical parameters used were tapping amplitude, set point 0.8 V with a 256 points per line, 1 Hz scan rate. X-ray scattering tests were performed using a PANalytical X'Pert Pro diffractometer with Cu-K_α radiation at room temperature. X-ray photoemission spectra (XPS) were measured with an X-ray photoemission spectroscopy instrument (ESCALAB 250Xi, Cavendish Laboratory). The polymer films were evacuated under vacuum of 10⁻¹⁰ mbar for one hour prior to moving to the chamber for measurement. The C-C peak at 284.8 eV was used as a charge correction reference. Gel permeation chromatography (GPC) analyses were performed either on chloroform solutions (2 mg ml⁻¹) using a GPC MAX variable loop equipped with two KF-805L SHODEX columns and a RI(VE3580) detector, operating at a flow rate of 1 ml min⁻¹, or on DMF solutions containing 0.1 wt% lithium bromide (5 mg ml⁻¹) using a high performance liquid chromatography system (Shimadzu, Prominence system) equipped with a pump (Shimadzu, LC-20AD), 3 columns including a guard column (Agilent Technologies, guard column: 1xPolarGel-M, separation columns: 1xPolarGel-M and 1xPolarGel-L) and a photodiode array detector (Shimadzu, SPD-M20A) at 60°C. Calibration was achieved using Viscotek polystyrene standards (*M_w* 1000 – 1,000,000 g mol⁻¹). Skeletal densities of polymer powders were measured using a Micromeritics Accupyc II 1340 helium pycnometer equipped with a 3.5 cm³ sample chamber at 25°C. Each sample was degassed at 110°C under vacuum for 12 h before measurement. A cycle of 10 measurements was performed to derive the mean value and standard deviation. Low-pressure gas physisorption was performed using a Micromeritics 3Flex surface characterization analyser. Each sample was degassed at 110°C under vacuum for 12 h, and then loaded into the apparatus and in-situ degassed at 110°C for another 12 h. Nitrogen adsorption isotherms were measured at 77 K and CO₂ adsorption isotherms measured at 273 K. Dynamic water vapor sorption was performed using a DVS Endeavour gravimetric sorption analyser (Surface Measurement Systems, UK) at 25°C. Polymer films (20-30 mg, about 50 μm thick) were dried *in vacuo* at 110°C for 12 h, and *in situ* dried under flowing dry air at room temperature for at least 24 h and when the mass became constant Water uptake (WU) was determined by measuring the weight changes of polymer membranes in dry and fully hydrated states. Membrane samples were dried at 110 °C under vacuum for 12 h, and then quickly weighed with a high-precision analytical balance to obtain the dry mass. These samples were immersed in deionized water at room temperature for 24 h. The mass of fully hydrated samples was measured after the excess surface water was quickly wiped off with tissue paper. WU was calculated according to the following equation: $WU(\%) = (W_{\text{hydrated}} - W_{\text{dry}}) / W_{\text{dry}} \times 100\%$ Where *W_{hydrated}* and *W_{dry}* are the masses of fully hydrated and dry membrane samples, respectively. The concentration of metal-ions in ion diffusion measurements were detected by inductively coupled plasma - optical emission spectrometry (ICP-OES). Before testing, the permeate aliquots were diluted in 2 wt% HNO₃. Ultraviolet-Vis spectra were measured using a UV-VIS spectrometer UV-1800 (Shimadzu) with a wavelength range of 190–800 nm at an interval of 0.5 nm. High powered decoupling (Hpdec) magic angle spinning (MAS) solid state ¹³C nuclear magnetic resonance (NMR) spectra were collected using a Bruker Avance III 600 MHz instrument using an adamantane reference. A spinning rate of 15 000 Hz was used with powder samples packed into a 3.2 mm zirconium rotor. Spectra were typically compiled from 4000 scans with a 6 s recycle delay.

SAXS/WAXS characterization. SAXS/WAXS experiments were performed at the APS 12ID-B and C station. The 2D SAXS/WAXS data were collected on a Pilatus 2 M and 300 K area detector (DECTRIS Ltd) with an incident energy of 12 KeV. The scattering vector, *q*, was calibrated using silver behenate.

Gas permeation tests. Pure gas permeation tests were carried out with H₂, CO₂, O₂, N₂ and CH₄ (research grade, BOC, UK) under a feed pressure of 4 bar at 22°C, using a constant-volume pressure-increase apparatus. The detailed procedure and analysis methods were reported in previous work.⁵⁵ The membrane was evacuated thoroughly with a vacuum pump before measurements. The gas permeability is derived from the volume of gas flowing across the membrane. Permeability (*P*) is expressed in Barrer (1 Barrer = 10⁻¹⁰ cm³ (STP) cm cm⁻² s⁻¹ cm Hg⁻¹). The ideal selectivity for a gas pair (A/B) is calculated from the ratio of their permeability.

Diffusion and crossover experiments. Ion diffusion and redox molecule crossover tests were carried out using stirred H-shaped cells. Membrane samples were sandwiched between two polydimethylsiloxane (PDMS) O-rings and sealed in the middle of H-cells using clips or screw claps. The effective area of membrane samples in the H-cell

was 1.54 cm². We used magnetic stirring in both feed and permeate solutions to alleviate concentration polarization near the membranes. In single salt dialysis diffusion tests, 50 ml 1 M salt solution (KCl, NaCl, LiCl, CaCl₂, MgCl₂, K₃Fe(CN)₆, K₄Fe(CN)₆, KOH, NaOH or LiOH) was used as the feed solution, and the permeate side was filled with 50 ml deionised water. The ionic conductivity of permeate solution was continuously recorded using an ionic conductivity meter (Thermo Scientific Orion Star A210) at a recording interval of 20 s. Afterwards, the concentration change of permeate solution over time was obtained based on the linear relationship between the conductivity and concentration of salt solutions. A series of salt solutions with various concentrations were prepared and their conductivities measured by conductivity meter to derive the calibration curves. The reliability of this conductivity method was confirmed by ICP-OES measurements. In the permeation measurements of interchanged cations, 1 M KCl solution was used as the feed with 1M NaCl, 1M LiCl, or 0.5 M MgCl₂ solution as the permeate, and PIM-EA-TB thin film as the membrane. In binary ion diffusion tests, 50 ml salt solution containing 0.5 M KCl and 0.5 M MgCl₂ was used as the feed solution, and the permeate side was filled with 50 ml deionised water. The concentrations of K⁺ and Mg²⁺ in permeate side were measured by ICP-OES. In single redox-specie crossover tests of redox molecules, redox active materials (2,6-DHAQ, FMN-Na or K₄Fe(CN)₆) dissolved in 1M NaOH aqueous solution were used as the feed solution and the volume was 50 ml; 50 ml 1M NaOH aqueous solution was used in the permeate side. The concentration change of the permeate solution was monitored and quantitatively measured by a calibrated UV-Vis spectrometer or ICP-OES. In contra-diffusion crossover tests of redox molecules, redox active materials (K₄Fe(CN)₆) dissolved in 1M NaOH aqueous solution were used as the feed solution and the volume was 50 ml; redox species (2,6-DHAQ) dissolved in 50 ml 1M NaOH aqueous solution was used in the permeate side. The concentration change of Fe in the permeate solution was monitored by ICP-OES, and the concentration change of 2,6-DHAQ in feed solution was quantitatively measured by a calibrated UV-Vis spectrometer. The concentration of these redox couples are same as those of redox solutions for battery tests.

In these concentration-driven diffusion and crossover tests, the increase of concentration in permeate solution over the initial period without any volume change follows Fick's first law. The permeation rates (i.e., flux) of ions and redox species across a membrane are calculated from:

$$J = \frac{V}{A} \left(\frac{\partial C}{\partial t} \right)$$

Where J is the flux, V is the volume of solution and A is the effective area of membranes. C and t are the concentration of permeate and diffusion time, respectively.

During the process with a constant flux, Fick's first law can be simplified as:

$$J = D \frac{C_1 - C_2}{l} = P(C_1 - C_2)$$

Where D is the permeability; C_1 and C_2 are the concentrations of feed and permeate solutions, respectively; l is the thickness of membranes; P is the permeance.

Nanofiltration experiments. In order to evaluate the transport properties of PIM membranes towards ions and redox species with varied sizes, nanofiltration tests were performed using a dead-end stirred cell (300 – 400 rpm) under a feed pressure of 5-10 bar at room temperature. The effective membrane area was 14.6 cm². Feed solution concentration was 500 mg L⁻¹ in deionised water for salt rejection tests, and 20 and 500 mg L⁻¹ in deionised water for redox species nanofiltration tests. Feed volume was 200 ml. Concentration of the feed and permeate solutions was analysed using a conductivity meter or a UV-Vis spectrometer. The water permeance (J , L m⁻² h⁻¹ bar⁻¹) was determined by the following equation: $J = V/(A \times t \times p)$, where V is the volume of permeate solutions; A is the effective area of membranes using in nanofiltration cells; t is the testing time; P is the applied pressure. The rejection (R_i) was calculated from $R_i = (1 - (C_{P,i}/C_{F,i})) \times 100\%$, where $C_{P,i}$ and $C_{F,i}$ correspond to the concentrations in the permeate and the feed, respectively.

Ionic conductivity measurements. Ionic conductivity of polymer membranes was measured by the electrochemical impedance spectra (EIS) using the potentiostat mode with an AC bias of 10 mV and a frequency range of 0.2 MHz - 10 Hz. Membrane samples were soaked in 1 M NaOH or NaCl aqueous solutions for 24 h prior to measurements. The membranes were then sandwiched between two stainless steel electrodes and sealed with coin cells (Type 2032). The assembly process was carried out in 1M NaOH or NaCl aqueous solution in order to avoid any air bubbles from being trapped in the cells. The ionic conductivity was calculated according to the following equation: $\sigma = L/(R_m \times A)$, where R_m is the ionic resistance, L is the membrane thickness, A is the active membrane area (2.00 cm²), respectively. Nyquist plots were fitted by an equivalent circuit (Z-view, Fig S21) to derive R_m . Membrane thickness was measured by a micrometer.

Cyclic Voltammetry. CV measurements were carried out using a Biologic SP-150 potentiostat. CV measurements of redox species were performed using a three-electrode configuration composed of a glassy carbon working electrode, a Pt counter electrode and a Ag/AgCl reference electrode (pre-soaked in 3 M KCl solution). A two-electrode configuration was used to study the electrochemical stability of polymers; lithium metal was used as

reference and counter electrodes, and PIM/conductive carbon/PVDF composite (6: 3: 1 by weight) was used as the working electrode. Lithium metal and PIM composite electrodes were assembled in coin cells (Type 2032) with lithium salt electrolytes. The scanning rate for both configuration was 10 mV s⁻¹.

Battery tests and crossover measurements of operating batteries

Full-cell tests were carried out using a cell hardware (Scribner Associates) consisting of poly(tetrafluoroethylene) (PTFE) frames, conductive graphite plates with flow fields, copper current collectors, and graphite felt electrodes (GFA6, SGL) with an effective geometric area of 5 cm². Electrolytes were fed into the cell at a flow rate of 100 ml min⁻¹ controlled by a peristaltic pump (Cole-Parmer).

Membranes were pretreated prior to full cell tests. Nafion[®] 212 membranes were heated to 80 °C in deionized water for 20 minutes and then soaked in 6% hydrogen peroxide solution for 35 minutes¹⁰. After pretreatment, Nafion[®] 212 membranes were stored in 0.1 M NaOH solution. Thin film composite membranes were pretreated in 1 M NaOH water/ethanol (50: 50 by weight) for 18 h and then washed thoroughly with deionized water. Thick self-supported PIM membranes were soaked in 1 M NaOH solution for 24 h.

Charging-discharging measurements were performed using an electrochemical station (Biologic SP-150 potentiostat) with a constant current density at room temperature. Depending on the electrochemical properties of redox species, cut-off voltages for K₄Fe(CN)₆|2,6-DHAQ, K₄Fe(CN)₆|FMN and K₄Fe(CN)₆|ZnCl₂ species were set as 0.5-2.0, 0.6-1.7, and 0.8-1.7 V, respectively. Electrochemical rate tests were performed at varied current densities of 20, 40, 60, 80 and 100 mA cm⁻². In long-term cycling tests, current density was 80 mA cm⁻² for K₄Fe(CN)₆|2,6-DHAQ and K₄Fe(CN)₆|FMN systems, and 20 mA cm⁻² for K₄Fe(CN)₆|ZnCl₂ system. Coulombic efficiency was calculated by ratio of the discharge capacity to the charge capacity. Energy efficiency was calculated by the ratio of average discharge energy to the average charge energy. Voltage efficiency was calculated by the ratio of average discharge voltage to the average charge voltage. In electrochemical polarization tests, linear galvanic sweep measurements were carried out using the FMN-Na|K₄Fe(CN)₆ system with a scanning rate of 10 mA s⁻¹ from -400 to 800 mA. Specific power density was derived from i-v curves.

We found that carbon electrodes have critical effects on the energy efficiency, for example, thermal treatment could enhance the redox reactions and increase the energy efficiency⁷. However, the batch thermal treatment processing can be slightly different resulting in different performance. Therefore, for consistent comparison of membrane performance, we used the same batch of fresh graphite felt electrodes without thermal treatment throughout this study. Crossover rates in the operating batteries: the crossover rates of 2,6-DHAQ through separators to catholytes were measured by Cyclic Voltammetry with a scanning rate of 10 mV s⁻¹. The crossover rates of K₄Fe(CN)₆ through separators to anolytes were measured by ICP-OES. The samples for ICP-OES tests were collected after a certain time and diluted for 200 times in 2.0 wt% HNO₃ solutions.

Electrolyte preparation. In alkaline RFBs, 0.1 M 2,6-DHAQ, 0.1 M DHBQ, or 0.06 M FMN-Na dissolved in 1M NaOH solution was used as the anolyte; 0.1 M K₄Fe(CN)₆ dissolved in 1M NaOH was used as the catholyte. Electrolyte volume was 10 ml. The theoretical specific capacity of these redox couples was 2.68 Ah L⁻¹, determined by the limiting electrolyte, *i.e.*, the catholyte. For the high-concentration 2,6-DHAQ cycling experiment, 0.4 M K₄Fe(CN)₆ and 0.25 M DHAQ were used as the electrolytes and gave a theoretical specific capacity of 10.7 Ah L⁻¹.

Molecular simulation. We generated three amorphous models of PIM-1, AO-PIM-1 and PIM-EA-TB polymers, using the Amorphous Cell module in Materials Studio 2018 (Dassault Systèmes BIOVIA). All polymer chains consisted of 30 monomer units and amorphous models were constructed with 20 polymer chains per simulation box, with all interactions defined by the polymer consistent forcefield (PCFF). The procedure for packing and equilibration are described in detail elsewhere⁵⁶. Void analysis was carried out using the software zeo++. This software uses a Voronoi decomposition to calculate the interconnectivity of a porous material's pore network with respect to a probe of a given size, and for that probe can also calculate the surface area, accessible volume, largest included sphere, pore limiting diameter and a distribution of pore sizes. In this work, a probe size of 1.55 Å, equivalent to the Van der Waals radius of N₂, was used to acquire all quantities except the pore size distribution. Furthermore, 0.85 Å probe was also used to probe all three polymers, due to the presence of ultramicropores and smaller channels.

In situ solid-state NMR tests. All polymer membranes were dried *in vacuo* at 120°C before transferring into an Ar glove box. The membranes were not exposed to air during transfer. The membranes were then fractured into small pieces and packed into 3.2 mm solid state NMR rotors in the glove box. The mass loadings of PIM-1, AO-PIM-1 32%, AO-PIM-1 56% and AO-PIM-1 100% membranes were 8.0, 11.6 mg, 13.0 and 13.8 mg, respectively. 20 wt% 1M NaOH aqueous solution was added into each of the above polymer membranes inside a rotor; these soaked membrane samples were then subjected to NMR measurements immediately. All solid-state ¹H and ²³Na NMR spectra were acquired on a 16.4 T Bruker Avance III spectrometer using a 3.2 mm HXY probe head. A single-pulse sequence was used to acquire magic-angle spinning (MAS) spectra with spinning frequencies of 15 kHz, recycle delays of 5 and 3 s (for ¹H and ²³Na, respectively), and radiofrequency (rf) field strengths of 142 kHz and 385 kHz, respectively. ¹H and ²³Na shifts were externally referenced to solid adamantane at 1.87 ppm and Na₂Ti₃O₇ at 3 ppm. To monitor the adsorption dynamics of H₂O and Na⁺, automated multiple single pulse experiments were performed with a time interval of 10 s. Spin-lattice relaxation (T₁) measurements of ¹H were performed using the saturation

recovery technique with 25 spectra with incremental t in the second-dimension and 50 saturation pulses. The integrated peak areas were fitted to $f(t)=I_0 \times [1-\exp(-t/T_1)]$ to obtain relaxation constant T_1 .

Data availability. The data shown in the plots and that support the findings of this study are available from the corresponding authors on reasonable request.

51. Song, J. et al. Linear high molecular weight ladder polymers by optimized polycondensation of tetrahydroxytetramethylspirobisindane and 1, 4-dicyanotetrafluorobenzene. *Macromolecules* **41**, 7411-7417 (2008).
52. Yang, Z. et al. Highly Conductive Anion-Exchange Membranes from Microporous Tröger's Base Polymers. *Angewandte Chemie International Edition* **55**, 11499-11502 (2016).
53. Song, Q. et al. Porous organic cage thin films and molecular - sieving membranes. *Advanced Materials* **28**, 2629-2637 (2016).
54. Cook, M., Gaffney, P.R.J., Peeva, L.G. & Livingston, A.G. Roll-to-roll dip coating of three different PIMs for Organic Solvent Nanofiltration. *Journal of Membrane Science* **558**, 52-63 (2018).
55. Song, Q. et al. Zeolitic imidazolate framework (ZIF-8) based polymer nanocomposite membranes for gas separation. *Energy & Environmental Science* **5**, 8359-8369 (2012).
56. Tocci, E. et al. Molecular Modeling and Gas Permeation Properties of a Polymer of Intrinsic Microporosity Composed of Ethanoanthracene and Tröger's Base Units. *Macromolecules* **47**, 7900-7916 (2014).